Applied Catalysis B: Environmental 306 (2022) 121142

Contents lists available at ScienceDirect

Applied Catalysis B: Environmental

journal homepage: www.elsevier.com/locate/apcatb

Nitrogen-defect induced trap states steering electron-hole migration in graphite carbon nitride

Wenlu Li [a], Zhen Wei [b,*], Kaijian Zhu [c], Weiqin Wei [d], Jun Yang [a], Jianfang Jing [a], David Lee Phillips [b,*], Yongfa Zhu [a,*]

[a] Department of Chemistry, Tsinghua University, Beijing 100084, PR China
[b] Department of Chemistry, University of Hong Kong, Pokfulam Road, Hong Kong, China
[c] PhotoCatalytic Synthesis Group, MESA+ Institute for Nanotechnology, University of Twente, P.O. Box 217, Enschede 7500 AE, The Netherlands
[d] College of Chemistry, Central China Normal University, Wuhan 430079, PR China

ARTICLE INFO

Keywords:
Graphite carbon nitride
Nitrogen defects
Photocatalysis
Trap states
Femtosecond transient absorption spectroscopy

ABSTRACT

Defect structures of semiconductors intrinsically regulate the trap states, excitons and active charge carriers for artificial photosynthesis systems. A g-C_3N_4 system with abundant nitrogen defects was prepared through a thermal polycondensation strategy to reveal the role of trap states and exhibited a 20-fold enhanced H_2 evolution efficiency relative to bulk g-C_3N_4 under visible light irradiation. Subsequent femtosecond transient absorption spectroscopy study found that the N-defect induced shallow trap states can capture photogenerated electrons to inhibit deep trapping and direct recombination of photogenerated charges. The active electrons in shallow trap states can enhance the photocatalytic H_2 evolution when compared with the inactive electrons in deep trap states. Mid-infrared transient absorption spectroscopy also confirmed the increased quantity of shallow-trapped electrons without interference of other signals. This work provides new insights for steering depth of trap states and photocatalytic processes through N defects to achieve high photocatalytic performance using femtosecond transient absorption spectroscopy.

1. Introduction

The increasingly serious environmental problems and declining fossil fuel reserves are great crisis of our society, which may be confronted by converting solar energy into carbon-neutral solar fuels, especially hydrogen fuel. Hydrogen is an ideal renewable fuel due to its clean fuel nature and high gravimetric energy density (120 $MJ \cdot kg^{-1}$, about 3 times higher than gasoline) [1]. In recent years, photocatalytic hydrogen production from water splitting has attracted considerable attentions due to its sustainable and economical properties [2]. Due to its high photocatalytic efficiency and stability, proper band structure, easy fabrication and low cost, g-C_3N_4 has become one of the most popular photocatalysts when it was first reported for visible-light-driven H_2 evolution [3–5]. Melem is the simplest heptazine-based molecule [6] and a good precursor for the synthesis of g-C_3N_4 [7–9]. Nitrogen defects in the framework of g-C_3N_4 have been reported to show a significant effect on the photocatalytic activity performances of g-C_3N_4 based systems and induced defect states have been found to make an indispensable contribution for visible light absorption and charge transfer in their photocatalytic processes [10–12]. However, the importance and detailed roles of trap states has not been fully realized due to some limitations of experiments and theory used to date. Nevertheless, the study of defect states and photogenerated charges in photocatalytic process are of continuing interest and attract the application of new experimental and theoretical methods to study them.

It is well known that a typical photocatalytic reaction mainly consists of photoexcitation, charge separation and transfer, and surface catalytic reactions [13]. Charge separation and transfer are the prerequisite kinetic factor to display the efficacy of the final catalytic reactions due to the disparity between the lifetimes of photoexcited charges (picosecond-nanosecond) and the timescale of surface reactions (millisecond--second) [14,15]. After separation, the free photogenerated electron-hole pairs can transfer to the surface of catalysts to react with molecules directly, but some of them may be trapped by some intermediate states (trap states) between the quasi-Fermi levels of the electrons and holes, which can limit the quasi-Fermi level splitting, and dominate photogenerated electron-hole recombination and transfer processes of the materials [16]. There are different trap states for electrons and they

* Corresponding authors.
E-mail addresses: xfwz522@126.com (Z. Wei), phillips@hku.hk (D.L. Phillips), zhuyf@mail.tsinghua.edu.cn (Y. Zhu).

https://doi.org/10.1016/j.apcatb.2022.121142
Received 14 November 2021; Received in revised form 10 January 2022; Accepted 21 January 2022
Available online 25 January 2022
0926-3373/© 2022 Elsevier B.V. All rights reserved.

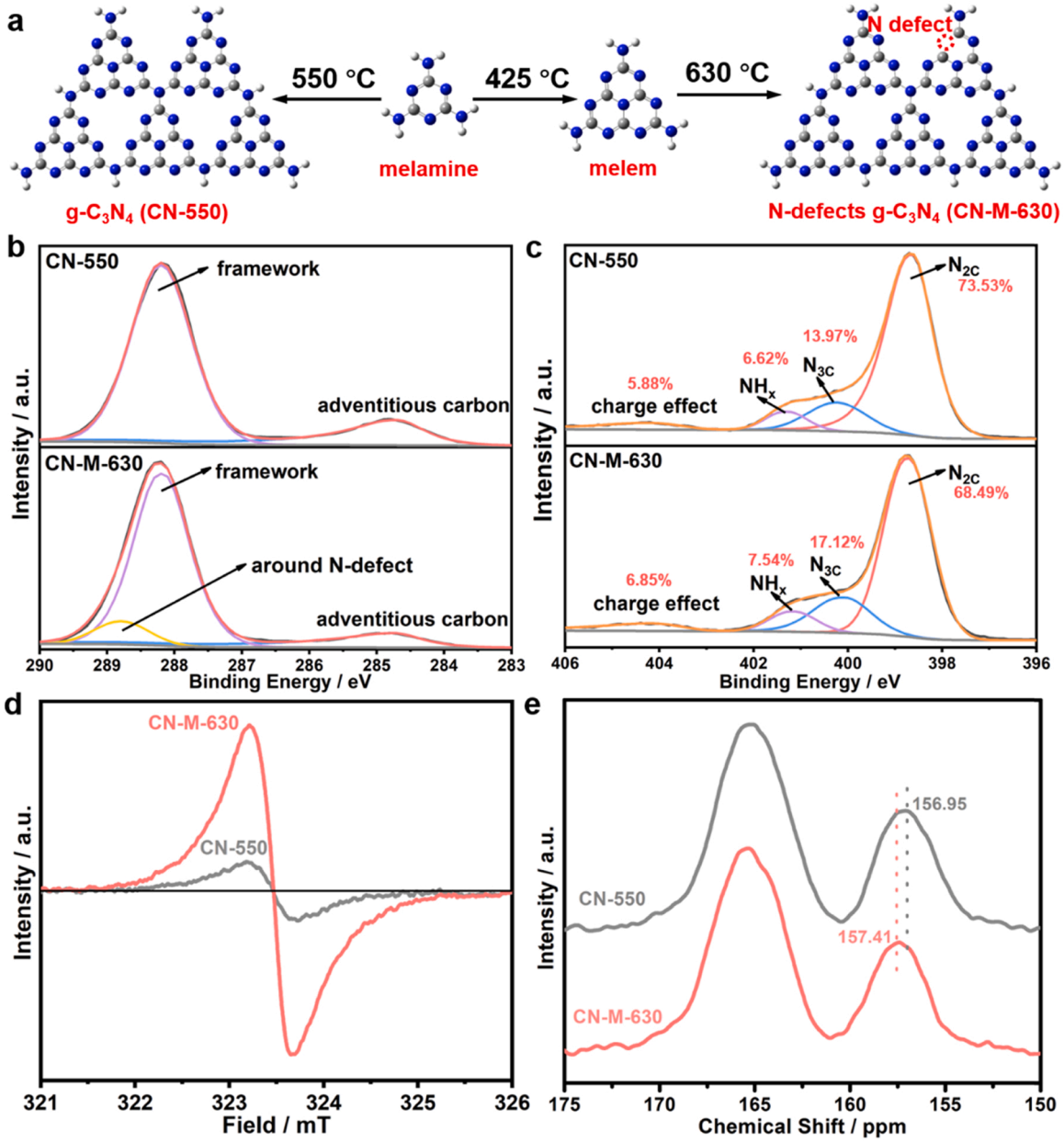

Fig. 1. (a) Schematic illustration for the fabrication of CN-550 and CN-M-630; XPS with peak for (b) C1s and (c) N1s of CN-550 and CN-M-630; (d) EPR spectra of CN-550 and CN-M-630; and (e) Solid-state ^{13}C CP-MAS NMR spectra of CN-550 and CN-M-630.

possess different energy differences (ΔE) between the trap state and the conduction band edge, which is the quantized support to distinguish shallow and deep trap states from each other [17]. A larger ΔE of the trap state signifies deeper trapping of photogenerated electrons and more positive reduction potential the trapped electrons [18]. As a consequence, deep trapping is disadvantageous to the transfer of charges and the subsequent photocatalytic reactions. It has been reported extensively that trap states of the semiconductors can be efficiently modulated by defect structures. Then some free electrons and even excitons may relax into trap states for which the depth will affect the activation of the photogenerated electrons and photocatalytic efficiency of catalysts. Some studies have found that shallow trap states electrons often possess good reactivity for the subsequent reactions. But for deep trap states, most of the energy of the electrons is lost so as to lead to a reduction in the driving force of catalytic reactions to limit the formation of target products [19].

Consequently, understanding such a trapping process and the effects of defect structures can help guide the design and engineering of new photocatalysts for highly efficient solar energy conversion. Ultrafast time-resolved spectroscopy serves as a direct and powerful tool in monitoring the carrier dynamics upon photoexcitation of photocatalysts because the formation, thermal relaxation, trapping, and recombination of photogenerated charges mostly occur on relatively fast scales (fs-ns) [20,21]. Such ultrafast transient absorption spectroscopy techniques have been widely used for probing the electron and hole behaviors and charge trap processes in solar cells and photocatalysis systems. Annamaria et al. reported that most electrons decayed through trapping and form surprisingly long lived trapped electrons in perovskite films, which can rationalize the high obtainable open-circuit voltage for perovskite solar cells [16]. And oxygen vacancies were found to be valuable to induce electron trapping states, which can inhibit the direct recombination of photogenerated carriers and thus improve photocatalytic oxygen evolution of tungsten oxides [22]. The trap states of g-C_3N_4 were also researched in several studies. Clear photocathode behavior of

N-defects g-C_3N_4 has been observed due to the shallow-trapped charges associated with both N-defects and C-OH terminal groups [23]. Deep trapped long-lived electrons can accumulate in g-C_3N_4 and cause large amounts of energy loss, resulting in the driving force decrease of charge transfer reactions [19]. The exfoliated C_3N_4 can quench photogenerated electrons on g-C_3N_4 with a rate approaching the molecular diffusion limit to enhance the photocatalytic H_2 production [24].

Herein, we built a series of N-defect g-C_3N_4 samples through a thermal polycondensation strategy for highly enhanced photocatalytic H_2 evolution and carried out a visible and mid-infrared femtosecond transient absorption spectroscopy study on the relationship between the electron trapping states and N defects. We found that N defects can introduce additional defect states for shallow trapping of photogenerated electrons, which can inhibit inactive deep trapping and direct recombination of photogenerated charges. This work provides insights into the study of defect structures and electron trapping of photocatalysis through the use of femtosecond transient absorption spectroscopy and offers some guidance for the design of efficient hydrogen evolution catalysts for the realization of advanced renewable energy schemes.

2. Experimental section

2.1. Synthesis of melem

10 g of melamine was placed in a porcelain crucible with a lid, heated at 2 °C/min to 425 °C for 4 h, and then cooled to room temperature. The white product was melem [25].

2.2. Synthesis of CN-x (x = 550, 600, 630) and CN-M-x (x = 550, 600, 630) series of samples

The g-C_3N_4 samples were prepared through a simple thermal polycondensation strategy by regulating the precursors and temperature as depicted in the scheme shown in Fig. 1a 0.5 g of melamine was placed in a porcelain boat with a lid, and heated to 550 °C, 600 °C, 630 °C, and 650 °C with the rate of 2.3 °C/min for 4 h under Ar atmosphere, respectively. The products obtained at 550 °C, 600 °C, and 630 °C were marked as CN-550, CN-600 and CN-630. When calcined at 650 °C, no products were obtained. CN-M-550, CN-M-600 and CN-M-630 were synthesized with melem as raw material under the same conditions. CN-550 was used as a bulk g-C_3N_4 sample.

2.3. Femtosecond transient absorption spectroscopy

The femtosecond transient absorption spectra were measured through a home-made system, of which the details and structure diagram (Fig. S1) are described in Supplementary Material. The samples were dispersed in water or 10% of methanol solution for visible probe (420–800 nm) and pressed into thin slices with KBr for mid-IR probe (4500–5100 nm). The samples were excited by a 400 nm pump beam.

2.4. Evaluation of photocatalytic H_2 evaluation performances

The photocatalytic H_2 evolution of the graphic carbon nitride samples were evaluated in an all glass automatic on-line trace gas analysis system (Labsolar-6A, Beijing PerfectLight, Fig. S2) with a Pyrex top-irradiation reaction vessel under visible light (43.8 mW/cm^2) irradiation with at 5 °C. The photocatalysts (25 mg) were added into 100 mL solution (90 mL of deionized water and 10 mL of triethanolamine as sacrificial agent). The concentration of generated H_2 was analyzed through an online gas chromatograph (GC-7800) with a thermal conductivity detector. More details are described in Supplementary Material.

Table 1
Elemental analysis of different samples.

Sample	N	C	H	C/N
CN-M-550	3.89	3	2.35	0.77
CN-M-600	3.85	3	2.34	0.78
CN-M-630	3.78	3	2.42	0.79
CN-550	3.97	3	2.36	0.76

3. Results and discussion

3.1. Structure of N-defect g-C_3N_4

The crystal structures of the g-C_3N_4 samples were recorded by powder X-ray diffraction (XRD) patterns (Fig. S3). All of the samples exhibited two diffraction peaks at 13.4° (100) and 27.3° (002), which attributed to the in-plane structure of the tri-s-triazine units and graphitic stacking, respectively [26]. The (002) peak of CN-550 was stronger than that of CN-M-550 due to their different thickness and stacking range, while CN-M-550 showed a stronger (100) peak because of its more complete in-plane structure of the tri-s-triazine units. With an increase of calcination temperature rising, both (002) and (100) peaks of the CN-M-x(x = 550, 600, 630) samples gradually became broader and weaker, which indicates that the structure of g-C_3N_4 was partly destroyed by the higher temperature, resulting in the formation of N-defects. The morphology of CN-550 and CN-M-630 were characterized by scanning electron microscope (SEM) and transmission electron microscope (TEM) in Figs. S4–S8 CN-500 displays a thick and layered structure and the size distribution is uneven, which is the typical morphology of bulk g-C_3N_4 [27]. However, CN-M-630 presents as thinner nanosheets with fluffy and porous structure, which can be measured through the atomic force microscope (AFM, Fig. S9) that the thickness is 3 nm, which is thinner than that of CN-550 (5 nm). The BET specific surface area and pore distribution of samples were measured by N_2 adsorption-desorption isotherms (Fig. S11 and Table S1). Both CN-550 and CN-M-630 were identified as type IV isotherms and the BET specific surface area of CN-M-630 was calculated to be 52.17 m^2/g, 7.78 times higher than that of CN-550 (6.71 m^2/g). And the pore sizes of CN-M-630 mainly locate on the mesoporous region (2–50 nm), and the pore density of CN-M-630 is obviously higher than that of CN-550. The porous structure is consistent with the results of SEM and TEM. The heating phase transformation of melamine and melem were analyzed with thermogravimetric-differential scanning calorimetry analysis (TGA-DSC) in Fig. S12 Melamine shows a sharp decrease of weight at 350 °C and a mild decrease from 500 to 700°C, while the primary weight loss of the as-prepared melem was located in the 500–700 °C region.

Theoretically, the standard C/N ratio of g-C_3N_4 should be 0.75. According to the elemental analysis results in Table 1, the C/N ratio of CN-550 and CN-M-630 are 0.756 and 0.793, respectively. The significantly reduced content of nitrogen element directly shows the loss of N element as the temperature rises, which may lead to the formation of nitrogen defects in the plane of tri-s-triazine. To reveal the type of N defects and structural changes associated with the N-defects of g-C_3N_4 further, high resolution X-ray photoelectron spectroscopy (XPS) of samples were measured to investigate the chemical states of elements. The N1s spectra (Fig. 1b) can be fitted by four peaks both in CN-550 and CN-M-630. The major peak at 398.6 eV is corresponding to two-coordinated nitrogen atoms (N_{2C}) in the framework of the heptazine unit, while the minor shoulder peaks at 400.2 and 401.3 eV can be attributed to three-coordinated nitrogen atoms (N_{3C}) and NH_x groups on the edge or between heptazine units, respectively. And the smallest peak at 404.1 eV is due to a charge effect [28]. The contents of different types of N were calculated from their peak areas in the XPS N1s spectra. It is apparent that the N_{2C} content of CN-M-630 (68.5%) lower than that of CN-550 (73.5%), indicating that the formation of N defects was mainly due to the loss of N_{2C} during the condensation process. Because the N_{2C} atoms

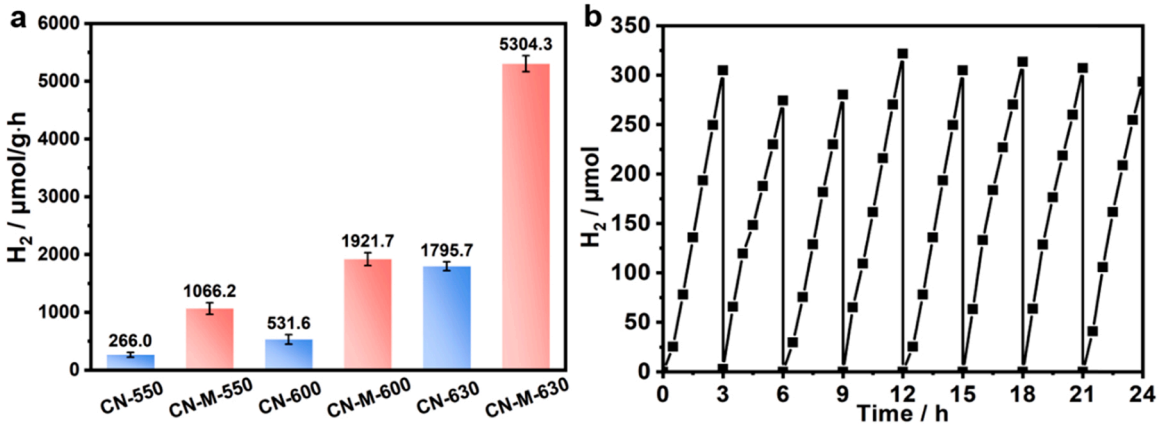

Fig. 2. (a) Photocatalytic H_2 evolution rates of different samples under visible irradiation ($\lambda > 420$ nm); (b) the repeated cycles of H_2 evolution by CN-M-630.

possess higher unsaturated coordination and population, they are easier to escape from the structure [29]. The N_{3C} content of CN-M-630 is 17.1%, higher than that of CN-550 (13.9%), which may contain the signal overlap of N_{3C} and cyano groups, whose binding energies are between those of N_{2C} and N_{3C} [28]. As to high resolution C1s XPS spectra (Fig. 1c), the dominant peak at 288.2 eV stems from the structural C in the framework of the heptazine units, and the minor peak at 284.8 eV mainly attributes to the adventitious carbon. Compared with CN-550, CN-M-630 exhibited a weak shoulder peak at 288.8 eV, which may be attributed to the C atoms around N-defect sites [10]. These results indicate that partial N_{2C} is preferentially removed during calcining at high temperature, resulting in the formation of N_{2C} defects and opening of the s-triazine heterocycle. Light absorption properties of the samples were also characterized by UV-Vis diffuse reflectance spectra (DRS) in Fig. S13. The intrinsic absorption edge of CN-M-630 locates at 480 nm, close to that of CN-550 (465 nm). However, a new red-shift absorption edge (577 nm) can be observed in CN-M-630, due to the present of defect states caused by N defects below the conduction band (CB) [30]. The N defects extend the visible light-harvesting range of CN-M-630, which is beneficial to improve its photocatalytic performances. Solid-state EPR was also used to confirm the various behaviors of the native defects of the samples (Fig. 1d). Both CN-550 and CN-M-630 have an obvious symmetrical resonance signal centered at g = 2.003, which can be attributed to the unpaired electrons of the aromatic rings. When N atoms are removed from the triazine rings, the extra electrons can be redistributed to the closest C atoms rapidly by the delocalized π-conjugated networks of g-C_3N_4 [31]. It is noticeable that a weak analogous signal is also detected for CN-550, because the structure of CN-550 is also not ideal.

The characteristic peaks of the Fourier transform infrared spectroscopy (FTIR) of CN-550 and CN-M-630 display almost no differences (Fig. S15). Characteristic bands over 900–1800 cm^{-1} can be corresponding to bridging C-NH-C units and full condensation trigonal $N(-C)_3$ features. The absorption band of C-N at 810 cm^{-1} is attributed to the

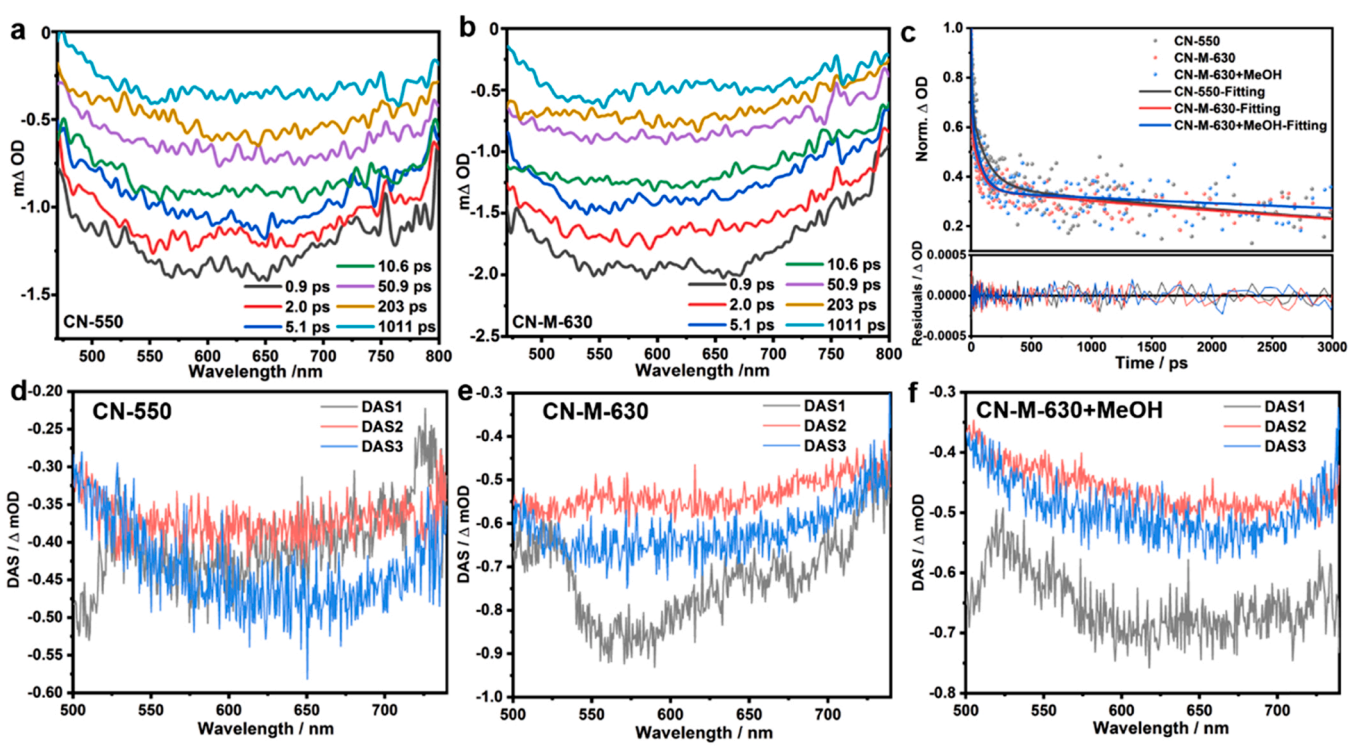

Fig. 3. Visible transient absorption spectra measurements of (a) CN-550, (b) CN-M-630 with a 400 nm laser flash, and (c) Time profiles of normalized transient absorption at 560 nm; global analysis of (d) CN-550; (e) CN-M-630 and (f) CN-M-630 in 10% of methanol with a parallel model.

Table 2
Kinetic parameters of the transient absorption decay of the samples.

Sample	Conditions	τ_1 / ps	τ_2 / ps	τ_3 / ps
CN-550	visible; water	7.4	123	6751 (∞*)
CN-M-630	visible; water	4.2	69	7232 (∞*)
CN-M-630	visible; 10% MeOH	4.9	76	13823 (∞*)
CN-550	MIR	4.3	119	1226
CN-M-630	MIR	2.3	47	707

* The fitted lifetime τ_3 has overflowed the range of instrument, so it can be seen as ∞.

bending mode of the heptazine rings, revealing the existence of the basic melon units with NH/NH_2 groups [32]. The characteristic breathing mode at around 3000–3500 cm^{-1} indicates the existence of primary amines and partial condensed secondary amines in the sample [33]. This peak shifted about 5 cm^{-1} toward high frequency in the spectrum of CN-M-630 compared with that of CN-550, which can be ascribed to the generation of nitrogen vacancies [34].

3.2. Photocatalytic H_2 evolution performances

Photocatalytic performances of the samples were characterized through photocatalytic H_2 evolution reaction from water splitting by using Pt (3 wt%) as cocatalyst and triethanolamine (TEOA) as a hole sacrifice under visible light irradiation (λ > 420 nm) in Fig. 2a H_2 evolution activity of g-C_3N_4 samples synthesized from melem exhibited a significant increase with the rise of the polymerization temperature (CN-M-630 > CN-M-600 > CN-M-550) due to the formation of N-defects. However, when the polymerization temperature rose to 650 °C, no product was obtained due to the decomposition of material under such a high temperature. At the same polymerization temperature, the sample with melem as precursor shows better photocatalytic H_2 evolution performance than melamine. The H_2 evolution rate of CN-M-630 achieved 5304.3 μmol·g^{-1}·h^{-1}, which is 20 times higher than that of CN-550 (266 μmol·g^{-1}·h^{-1}). The apparent quantum yield (AQY) of H_2 evolution were measured to obtain a more objective measure for solar energy conversion efficiency of the samples (Fig. S16). With the introduction of N-defects, the AQY CN-M-630 at 420 nm is enhanced to 15.7%, while that of CN-550 is only 4.2%. Significantly, the AQY at 450 and 500 nm increase to 3.8% and 2.1%, presenting a remarkable improvement when compared to CN-550 (<1%). In order to inspect the photocatalytic stability of CN-M-630, we tested its H_2 evolution performance circularly. As the H_2 evolution cycling curves shown in Fig. 2b, CN-M-630 exhibits no obvious decrease in H_2 evolution cycling process for eight runs. These results indicate that CN-M-630 is stable for the photocatalytic water splitting, which is significant for its practical applications.

3.3. Shallow trap of photogenerated electrons

To obtain an in-depth understanding on the influence of N-defects in CN-M-630 on photocatalytic H_2 evolution, femtosecond transient absorption (fs-TA) spectroscopy was performed on CN-550 and CN-M-630 samples, which is a robust tool for tracking in real time the relaxation kinetics of photogenerated charge carriers in semiconductor systems. We chose a pump-probe configuration with a 400 nm pump and a visible probe (480–800 nm) to trace the photogenerated electron kinetics [35]. Both CN-550 and CN-M-630 exhibit only negative TA signals in the visible probe region at select time points from 0.9 ps to 1011 ps (Fig. 3a, b), which can be attributed to the overlap of electron and hole absorption on the heptazine framework, stimulated emission and ground-state bleach [23,24]. The decay kinetics of the overlapping signals are difficult to be fitted just through a multi-exponential function, so we performed a global analysis of the spectrum through the parallel model to study the decay process of photogenerated electrons. Fig. 3c exhibits the TA decay kinetics at 560 nm for CN-550 and CN-M-630, of which the fitting residuals demonstrate the feasibility of the modeling and the model used has high-precision and appears to fit the data well. CN-M-630 shows obviously faster decay than CN-550 in 1 ns and a similar decay at longer time. The TA data of the samples yield three decay-associated spectra (DAS) and converge well in the global analysis employed here (Fig. 3d–e). The fitting results shown in Table 2 for CN-550 provides decay lifetimes of the three spectral components to be τ_1 = 7.4 ps, τ_2 = 123 ps, and τ_3 = 6715 ps, while CN-M-630 shows analogous results of τ_1 = 4.2 ps, τ_2 = 69 ps, and τ_3 = 7323 ps. The shorter lifetimes of the spectral components τ_1 and τ_2 attributes to the electrons relaxation process from CB to different trap states, while the longer lifetime τ_3 corresponds to the recombination of photogenerated charges [36]. The band structure of CN-M-630 can be changed due to the introduction of N defects, where some defects states are formed below the CB. The CB and valence band (VB) of CN-M-630 can be measured to be − 0.73 and 1.85 V versus reversible hydrogen electrode at pH= 7 (RHE, pH=7) according to the electrochemical Mott-Schottky (MS) plots (Fig. S17) and DRS(Fig. S13a) [37]. The additional absorption edge at 577 nm implies that the defect states mainly distribute between −0.73 and −0.30 V (RHE, pH=7). The defect states close to the CB can trap photogenerated electrons from CB and the trapped electrons can react with water for the additional production of H_2. The electron trapped by defect states are shallow-trapped electrons and the defect states are main components of shallow trap states for CN-M-630 in photocatalytic processes [38]. For the short lifetimes τ_1 and τ_2, τ_1 suggests a faster decay for the intermediate trapping of the photogenerated electrons in the excitonic states [35]. CN-M-630 exhibits shorter τ_1 (4.2 ps) than CN-550 (7.4 ps) due to the effects of defect states. And the τ_2 of CN-M-630 attributes to the electron relaxations to the N-defects induced shallow trap states. However, τ_2 of CN-550 (123 ps) is nearly twice longer than that of CN-M-630 (69 ps), indicating the presence deeper trap of electrons,

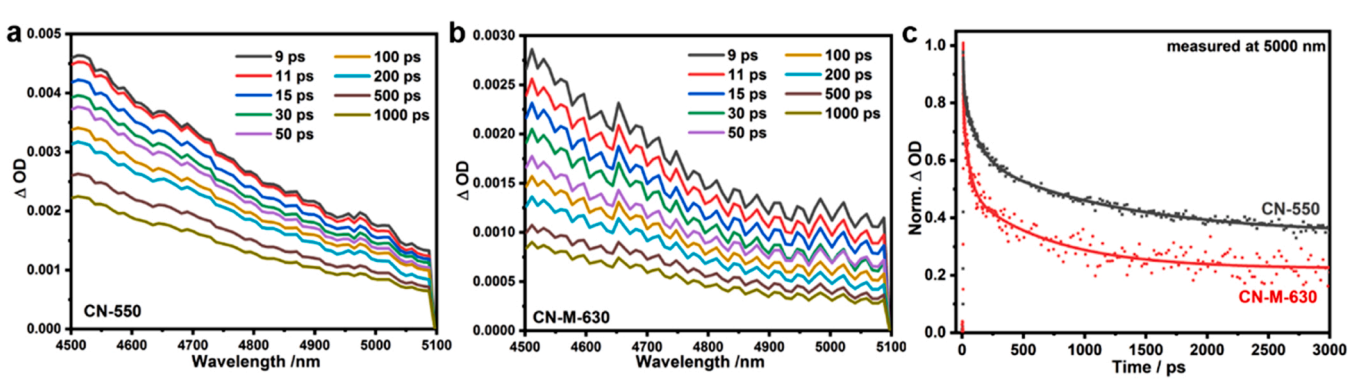

Fig. 4. MIR fs-TAS for (a) CN-550 and (b) CN-M-630 irradiated with pulses at 400 nm; and (c) MIR fs-TAS decay kinetics at 5000 nm of CN-550 and CN-M-630 powder samples.

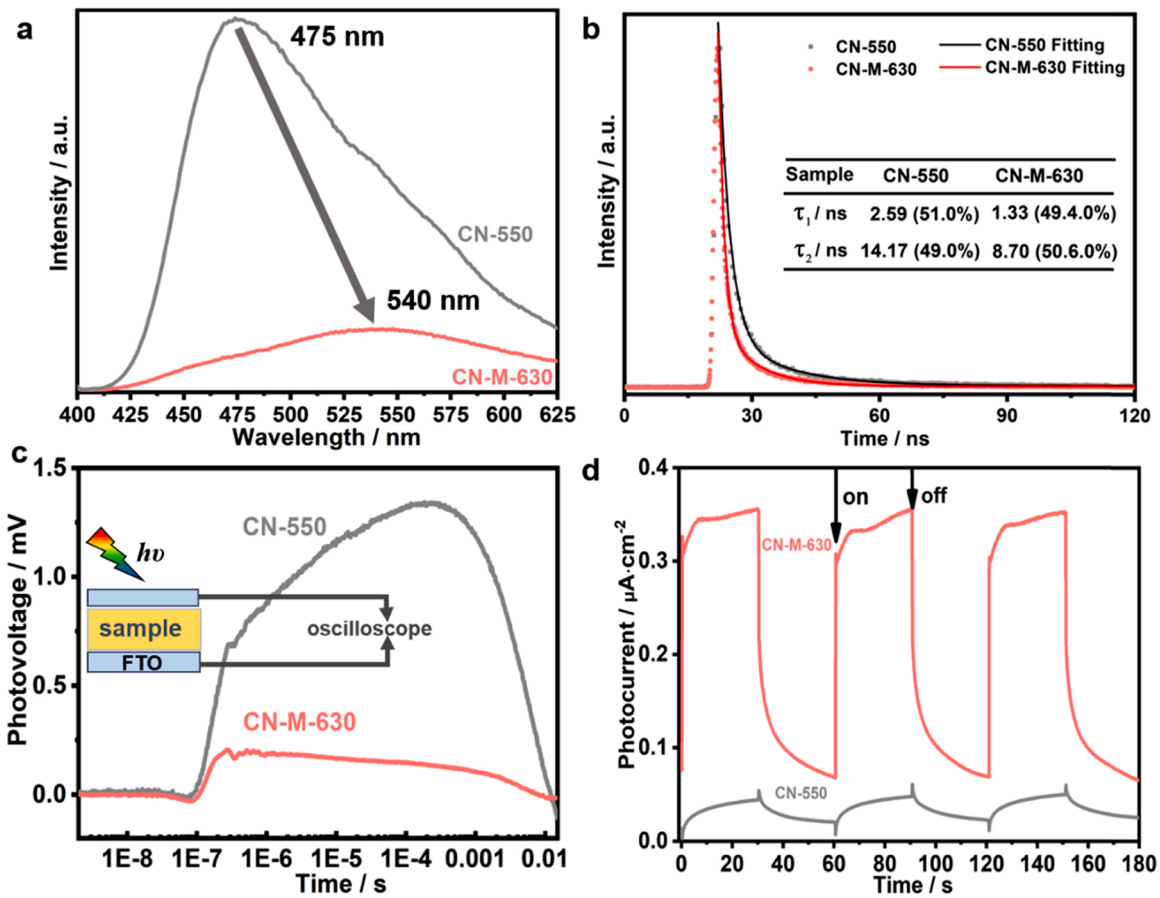

Fig. 5. (a) PL spectra of CN-550 and CN-M-630 excited at 365 nm; (b) transient fluorescence of CN-550 and CN-M-630 recorded at 470 nm (excited by 325 nm excitation pulse); (c) TPV measurements of CN-550 and CN-M-630, where the wavelength and intensity of the excitation pulse are 355 nm and 50 mJ, respectively; (d) transient photocurrent response of the as-prepared CN-550 and CN-M-630. (FTO: fluorine-doped tin oxide glass).

which are inactive for photocatalytic reactions due to the spatial confinement and potential of deeply trapped electrons [39]. These results demonstrate that the N-defects in CN-M-630 can induce shallow trapped states for the trapping of photoelectrons to boost the exciton dissociation and improve photocatalytic H_2 evolution performances [40].

Furthermore, we determined the photoinduced electron characters affected by hole capture using a 10% methanol solution as a hole scavenger in the CN-M-630 system and the fs-TA spectra show similar absorption bands (Fig. S17). Compared with dispersion in pure water, CN-M-630 exhibits a slower decay in the 10% methanol solution after global analysis, especially for the recombination process (Fig. 3c and f). The shorter lifetime τ_1 (4.9 ps) and τ_2 (76 ps) just show a slight delay, indicating that hole capture has little influence on the electron trapping of shallow trap states. The lifetime of the third spectral components (τ_3) is prolonged to 13.8 ns due to the photogenerated hole capture of methanol, which can restrain the recombination of photogenerated charges [19,41].

Compared with the absorption observed in the visible range, mid-infrared femtosecond transient absorption (MIR fs-TA) spectroscopy does not contain the bleach signal and fluorescence signal of the ground state so the electronic dynamic signals there will not be affected by the mixed and indistinguishable signals seen in the visible region. Additionally, the mid-infrared absorption spectra of free carriers, trapped states carriers and impurity states have different spectral distributions, so the free carriers and trapped states carriers can be distinguished by the absorption spectrum lines in the MIR [42,43]. Therefore, MIR fs-TA is carried out to further study the photogenerated electron dynamics of CN-550 and CN-M-630 irradiated with photoexcitation at 400 nm. Obviously, both spectra show relatively strong absorption bands within the mid-IR region of 4500~5100 nm (Fig. 4a, b), which can be ascribed to the trapped electrons [44]. The decay kinetics of photogenerated electrons in CN-550 and CN-M-630 were tested by recording the changes in the transient absorption intensity at 5000 nm after photoexcitation (Fig. 4c). Such a decay can be fitted by the multi-exponential function, and the resultant fitting time constants are summarized in Table 2. It is obvious that CN-M-630 exhibits faster decay than CN-550. The longer lifetime τ_3 of CN-M-630 is 707 ps while that of CN-550 is 1226 ps, possibly corresponding to the long-lived deep-trapped electrons, which are inactive for photocatalytic reactions. And τ_1 (2.3 ps) and τ_2 (47 ps) of CN-M-630 are also much shorter than those of CN-550 (4.3 ps for τ_1 and 119 ps for τ_2), which can be attributed to the different shallow trapped electrons. This suggests electrons trapped in shallower trap states on the surface of the CN-M-630 sample, as these electrons have much shorter lifetime. These results demonstrate that N-defects induced shallow trap states can maintain the activation of the photogenerated electrons and promote the photocatalytic H_2 evolution of CN-M-630.

3.4. Charge transfer mechanism

Based on the H_2 evolution performances and fs-TA analysis of the samples, some insight into the charge transfer mechanism has been gained. In order to gain additional insights, photoluminescence (PL) spectra, time-resolved PL spectra, photo-electrochemistry tests, and transient photovoltage (TPV) were applied further to study the relationship between the defects, trap states and photogenerated charges. PL spectra of CN-550 and CN-M-630 were recorded with 365 nm excitation in Figs. 5a and S18–S19 CN-550 exhibits a strong and broad emission

signal with a peak at 475 nm, which can be attributed to the band-band recombination of photogenerated charge carriers, consistent with the band gap of CN-550. However, the emission signal of CN-M-630 represented an obvious quenching compared with CN-550, demonstrating there is an inhibition of charge recombination process due to the shallow trapping of photogenerated electrons [24]. In addition, the emission peak of CN-M-630 displays a strong red shift toward 540 nm, which attributes to the recombination from defect states to VB [28]. Time-resolved PL spectra (Fig. 5b) were collected to gain a deeper insight into the charge-transfer dynamics, where a biexponential fitting was applied to analyze the luminescence decay curves due to their complexity [45]. The shorter lifetime τ_1 attributes to the radiative decay of exciton from CB or defect states to VB, while the longer lifetime τ_2 is due to nonradiative decay of photogenerated charges [46]. The lifetimes of CN-M-630 (Fig. 5b) for the two processes both became shorter (τ_1, 1.33 vs 2.59 ns; τ_2, 8.70 vs 14.17 ns), which may be attributed to the appearance of a rapid radiative decay of photogenerated electrons related to the N-defect induced shallow trap states and shortened transfer distance by thinner nanosheets in CN-M-630 [47]. Nevertheless, the contribution of shorter lifetime only decreased from 51.0% to 49.4%, indicating lower quantity of quickly recombined charge carriers and better charge transfer and separation in CN-M-630 [48]. Therefore, CN-M-630 exhibited a shorter average lifetime than CN-550 (5.06 ns vs. 8.26 ns). TPV spectrum of CN-550 and CN-M-630 were measured to reveal the transfer dynamics of the photogenerated charge carriers further in Fig. 5c. They both showed an obvious positive signal at approximately 10^{-7}–10^{-2} s, which corresponds to the surface photovoltage from the drift of the photogenerated charges (10^{-7}–10^{-6} s) and exhibit a typical diffusion photovoltage (10^{-6}–10^{-2} s) [49]. Compared with CN-550, the signal intensity of CN-M-630 was weaker, owing to the increased electron trapping of shallow trap states caused by N defects [50]. And the small negative signal at about 10^{-7} s is attributed to the photogenerated electrons being transferred to the surface of the samples. The stronger peak intensity of CN-M-630 indicates that more photogenerated electrons can transfer to the surface at this timescale, resulting in a higher separation efficiency.

Photocurrent and electrochemical impedance spectra (EIS) were measured to further illustrate the effect of N defects on electron-hole separation efficiency in 0.1 M Na_2SO_4 solution. The photocurrent density of CN-550 was only 0.25 μA/cm^2, while it increased 10.8 times for CN-M-630 (0.023 μA/cm^2) with on/off visible light irradiation cycles (see Fig. 5d). And CN-M-630 also possesses a smaller Nyquist plots radius than CN-550 in the EIS spectra (Fig. S24), indicating it has a lower charge-transfer resistance in the CN-M-630 system which ensures the faster electron transfer [51]. When irradiated by visible light, the radius of Nyquist plots turns smaller in comparison with dark cases, indicating that light irradiation can enhance the charge separation and transfer process further. The linear sweep voltammetry (LSV) of CN-550 and CN-M-630 were tested to investigate their photo-electrocatalytic H_2 evolution capability thermodynamically (Fig. S25). CN-M-630 showed more positive hydrogen evolution onset potential than CN-550, indicating it has a lower H_2 evolution overpotential. Lower overpotential for CN-M-630 means that lower activation energy is needed for HER ($2\,H^+(aq.) + 2e^- = H_2(g)$) [52], leading to higher photocatalytic hydrogen production performance. CN-M-630 also presents higher current density than CN-550 no matter whether it is in dark or light circumstance at the same potential, which indicates that CN-M-630 exhibits a faster charge transfer rate. These photo-electrochemical results certified the improved separation and migration of photoinduced charges due to shallow trapped electrons caused by N defects in CN-M-630, thus bringing about the distinct performance of photocatalytic H_2 evolution.

Based on all the results above, we can demonstrate that the of N-defects could introduce shallow trap states to inhibit the recombination of photogenerated charges and this helps promote the reduction of H_2O on the surface of CN-M-630. The mechanism of the photocatalytic process is illustrated in Fig. 6.

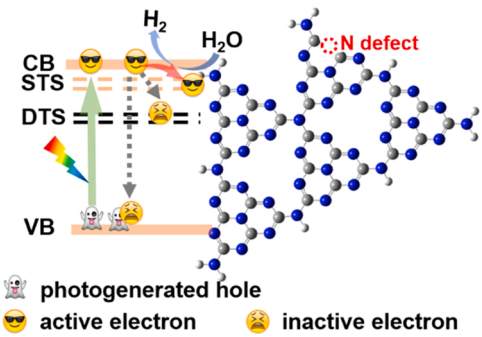

Fig. 6. The scheme of the photocatalytic mechanism of CN-M-630. (STS: shallow trap states; DTS: deep trap states).

4. Conclusions

In summary, we designed a N-defects g-C_3N_4 system via a thermal polycondensation strategy by regulating the precursors and temperature. Through the use of femtosecond transient absorption spectroscopy, we found that the N defects can steer the trap states of CN-M-630 for shallow trapping of electrons to inhibit photogenerated electrons from deep trapping and direct recombination, resulting in higher separation and transfer efficiency of photogenerated electron-hole pairs. And the shallow trapped electrons are active for reduction of H_2O into H_2, therefore CN-M-630 exhibits a significantly improved photocatalytic H_2 evolution rate of 5304.3 μmol·g^{-1}·h^{-1} under visible light irradiation, which is 20 times higher than that of bulk CN-550 (266 μmol·g^{-1}·h^{-1}). This work provides a novel concept for the relationship among defect structures, trap states and photocatalytic performances of semiconductors, and offers an idea for using ultrafast spectroscopy to examine photocatalytic reactions.

CRediT authorship contribution statement

Wenlu Li: design, Validation, Methodology, experiments, data analysis, Writing – original draft, Writing – review & editing, **Zhen Wei:** Supervision, Methodology, data analysis, Writing – original draft, Writing – review & editing. **Kaijian Zhu:** data analysis, writing–review. **Weiqin Wei:** Visualization, writing–review, **Jun Yang:** Visualization, writing–review. **Jianfang Jing:** Visualization, writing–review, **David Lee Phillips:** Supervision, Resources, Writing – review & editing. **Yongfa Zhu:** Supervision, Resources, Writing – review & editing,

Declaration of Competing Interest

The authors declare that they have no known competing financial interests or personal relationships that could have appeared to influence the work reported in this paper.

Acknowledgements

The authors are grateful for the financial grants from National Natural Science Foundation of China (21872077, 21621003), National Key Research and Development Project of China (2020YFA0710304), the Hong Kong Research Grants Council (GRF 17302419), The University of Hong Kong Development Fund 2013–2014 project "New Ultrafast Spectroscopy Experiments for Shared Facilities", Major Program of Guangdong Basic and Applied Research (2019B030302009), and Guangdong-Hong Kong-Macao Joint Laboratory of Optoelectronic and Magnetic Functional Materials (2019B121205002).

Appendix A. Supporting information

Supplementary data associated with this article can be found in the online version at doi:10.1016/j.apcatb.2022.121142.

References

[1] G. Zhang, Z.-A. Lan, X. Wang, Conjugated polymers: catalysts for photocatalytic hydrogen evolution, Angew. Chem. Int. Ed. 55 (2016) 15712–15727.
[2] L. Luo, Z. Gong, J. Ma, K. Wang, H. Zhu, K. Li, L. Xiong, X. Guo, J. Tang, Ultrathin sulfur-doped holey carbon nitride nanosheets with superior photocatalytic hydrogen production from water, Appl. Catal. B 284 (2021), 119742.
[3] X. Wang, K. Maeda, A. Thomas, K. Takanabe, G. Xin, J.M. Carlsson, K. Domen, M. Antonietti, A metal-free polymeric photocatalyst for hydrogen production from water under visible light, Nat. Mater. 8 (2009) 76–80.
[4] W. Luo, X. Chen, Z. Wei, D. Liu, W. Yao, Y. Zhu, Three-dimensional network structure assembled by g-C_3N_4 nanorods for improving visible-light photocatalytic performance, Appl. Catal. B 255 (2019), 117761.
[5] H. Wang, Y. Wu, M. Feng, W. Tu, T. Xiao, T. Xiong, H. Ang, X. Yuan, J.W. Chew, Visible-light-driven removal of tetracycline antibiotics and reclamation of hydrogen energy from natural water matrices and wastewater by polymeric carbon nitride foam, Water Res. 144 (2018) 215–225.
[6] J. Wen, R. Li, R. Lu, A. Yu, Photophysics and photocatalysis of melem: a spectroscopic reinvestigation, Chem. Asian J. 13 (2018) 1060–1066.
[7] J. Xia, G. Mark, M. Volokh, Y. Fang, H. Chen, X. Wang, M. Shalom, Supramolecular organization of melem for the synthesis of photoactive porous carbon nitride rods, Nanoscale 13 (2021) 19511–19517.
[8] J. Xia, N. Karjule, B. Mondal, J. Qin, M. Volokh, L. Xing, M. Shalom, Design of melem-based supramolecular assemblies for the synthesis of polymeric carbon nitrides with enhanced photocatalytic activity, J. Mater. Chem. A 9 (2021) 17855–17864.
[9] T.-G. Lee, H.-J. Kang, J.-H. Kim, N. Suzuki, A. Fujishima, M. Choi, Y.-S. Jun, Eutectic iodide-based salt as a melem-to-PTI conversion stopping agent for all-in-one graphitic carbon nitride, Appl. Catal. B 294 (2021), 120222.
[10] Q. Tay, P. Kanhere, C.F. Ng, S. Chen, S. Chakraborty, A.C.H. Huan, T.C. Sum, R. Ahuja, Z. Chen, Defect engineered g-C_3N_4 for efficient visible light photocatalytic hydrogen production, Chem. Mater. 27 (2015) 4930–4933.
[11] H. Sun, K. Wei, D. Wu, Z. Jiang, H. Zhao, T. Wang, Q. Zhang, P.K. Wong, Structure defects promoted exciton dissociation and carrier separation for enhancing photocatalytic hydrogen evolution, Appl. Catal. B 264 (2020), 118480.
[12] V.W.-h Lau, I. Moudrakovski, T. Botari, S. Weinberger, M.B. Mesch, V. Duppel, J. Senker, V. Blum, B.V. Lotsch, Rational design of carbon nitride photocatalysts by identification of cyanamide defects as catalytically relevant sites, Nat. Commun. 7 (2016) 12165.
[13] F. Chen, T. Ma, T. Zhang, Y. Zhang, H. Huang, Atomic-level charge separation strategies in semiconductor-based photocatalysts, Adv. Mater. 33 (2021), 2005256.
[14] S. Corby, R.R. Rao, L. Steier, J.R. Durrant, The kinetics of metal oxide photoanodes from charge generation to catalysis, Nat. Rev. Mater. 6 (2021) 1–20.
[15] C.S. Ponseca, P. Chábera, J. Uhlig, P. Persson, V. Sundström, Ultrafast electron dynamics in solar energy conversion, Chem. Rev. 117 (2017) 10940–11024.
[16] T. Leijtens, G.E. Eperon, A.J. Barker, G. Grancini, W. Zhang, J.M. Ball, A.R. S. Kandada, H.J. Snaith, A. Petrozza, Carrier trapping and recombination: the role of defect physics in enhancing the open circuit voltage of metal halide perovskite solar cells, Energy Environ. Sci. 9 (2016) 3472–3481.
[17] J. Jiang, C. Ling, T. Xu, W. Wang, X. Niu, A. Zafar, Z. Yan, X. Wang, Y. You, L. Sun, J. Lu, J. Wang, Z. Ni, Defect engineering for modulating the trap states in 2D photoconductors, Adv. Mater. 30 (2018), 1804332.
[18] R. Doolen, R. Laitinen, F. Parsapour, D.F. Kelley, Trap state dynamics in MoS_2 nanoclusters, J. Phys. Chem. B 102 (1998) 3906–3911.
[19] R. Godin, Y. Wang, M.A. Zwijnenburg, J. Tang, J.R. Durrant, Time-resolved spectroscopic investigation of charge trapping in carbon nitrides photocatalysts for hydrogen generation, J. Am. Chem. Soc. 139 (2017) 5216–5224.
[20] Z. Guo, Y. Wan, M. Yang, J. Snaider, K. Zhu, L. Huang, Long-range hot-carrier transport in hybrid perovskites visualized by ultrafast microscopy, Science 356 (2017) 59–62.
[21] Y. Li, Q. Wu, Y. Chen, R. Zhang, C. Li, K. Zhang, M. Li, Y. Lin, D. Wang, X. Zou, T. Xie, Interface engineering Z-scheme Ti-Fe_2O_3/In_2O_3 photoanode for highly efficient photoelectrochemical water splitting, Appl. Catal. B 290 (2021), 120058.
[22] Z. Wei, W. Wang, W. Li, X. Bai, J. Zhao, E.C.M. Tse, D.L. Phillips, Y. Zhu, Steering electron–hole migration pathways using oxygen vacancies in tungsten oxides to enhance their photocatalytic oxygen evolution performance, Angew. Chem. Int. Ed. 60 (2021) 8236–8242.
[23] Q. Ruan, T. Miao, H. Wang, J. Tang, Insight on shallow trap states-introduced photocathodic performance in n-type polymer photocatalysts, J. Am. Chem. Soc. 142 (2020) 2795–2802.
[24] K.L. Corp, C.W. Schlenker, Ultrafast spectroscopy reveals electron-transfer cascade that improves hydrogen evolution with carbon nitride photocatalysts, J. Am. Chem. Soc. 139 (2017) 7904–7912.
[25] S. Chu, C. Wang, J. Feng, Y. Wang, Z. Zou, Melem: a metal-free unit for photocatalytic hydrogen evolution, Int. J. Hydrog. Energy 39 (2014) 13519–13526.
[26] G. Zhang, S. Zang, X. Wang, Layered $Co(OH)_2$ deposited polymeric carbon nitrides for photocatalytic water oxidation, ACS Catal. 5 (2015) 941–947.
[27] G. Liao, Y. Gong, L. Zhang, H. Gao, G.-J. Yang, B. Fang, Semiconductor polymeric graphitic carbon nitride photocatalysts: the "holy grail" for the photocatalytic hydrogen evolution reaction under visible light, Energy Environ. Sci. 12 (2019) 2080–2147.
[28] S. Wu, H. Yu, S. Chen, X. Quan, Enhanced photocatalytic H_2O_2 production over carbon nitride by doping and defect engineering, ACS Catal. 10 (2020) 14380–14389.
[29] P. Niu, G. Liu, H.-M. Cheng, Nitrogen vacancy-promoted photocatalytic activity of graphitic carbon nitride, J. Phys. Chem. C 116 (2012) 11013–11018.
[30] H. Yu, R. Shi, Y. Zhao, T. Bian, Y. Zhao, C. Zhou, G.I.N. Waterhouse, L.-Z. Wu, C.-H. Tung, T. Zhang, Alkali-assisted synthesis of nitrogen deficient graphitic carbon nitride with tunable band structures for efficient visible-light-driven hydrogen evolution, Adv. Mater. 29 (2017), 1605148.
[31] Z. Hong, B. Shen, Y. Chen, B. Lin, B. Gao, Enhancement of photocatalytic H_2 evolution over nitrogen-deficient graphitic carbon nitride, J. Mater. Chem. A 1 (2013) 11754–11761.
[32] B.V. Lotsch, M. Döblinger, J. Sehnert, L. Seyfarth, J. Senker, O. Oeckler, W. Schnick, Unmasking melon by a complementary approach employing electron diffraction, solid-state NMR spectroscopy, and theoretical calculations—structural characterization of a carbon nitride polymer, Chem. Eur. J. 13 (2007) 4969–4980.
[33] M.J. Bojdys, J.-O. Müller, M. Antonietti, A. Thomas, Ionothermal synthesis of crystalline, condensed, graphitic carbon nitride, Chem. Eur. J. 14 (2008) 8177–8182.
[34] C.-Q. Xu, K. Li, W.-D. Zhang, Enhancing visible light photocatalytic activity of nitrogen-deficient g-C_3N_4 via thermal polymerization of acetic acid-treated melamine, J. Colloid Interface Sci. 495 (2017) 27–36.
[35] H. Wang, D. Yong, S. Chen, S. Jiang, X. Zhang, W. Shao, Q. Zhang, W. Yan, B. Pan, Y. Xie, Oxygen-vacancy-mediated exciton dissociation in BiOBr for boosting charge-carrier-involved molecular oxygen activation, J. Am. Chem. Soc. 140 (2018) 1760–1766.
[36] J. Xue, M. Fujitsuka, T. Majima, Shallow trap state-enhanced photocatalytic hydrogen evolution over thermal-decomposed polymeric carbon nitride, Chem. Commun. 56 (2020) 5921–5924.
[37] Z. Wei, W. Li, J. Hu, X. Ma, Y. Zhu, Interfacial internal electric field and oxygen vacancies synergistically enhance photocatalytic performance of bismuth oxychloride, J. Hazard. Mater. 402 (2021), 123470.
[38] J. Zheng, Y. Lyu, C. Xie, R. Wang, L. Tao, H. Wu, H. Zhou, S. Jiang, S. Wang, Defect-enhanced charge separation and transfer within protection layer/semiconductor structure of photoanodes, Adv. Mater. 30 (2018), 1801773.
[39] F. Liu, R. Shi, Z. Wang, Y. Weng, C.-M. Che, Y. Chen, Direct Z-scheme hetero-phase junction of black/red phosphorus for photocatalytic water splitting, Angew. Chem. Int. Ed. 58 (2019) 11791–11795.
[40] H. Wang, W. Liu, X. He, P. Zhang, X. Zhang, Y. Xie, An excitonic perspective on low-dimensional semiconductors for photocatalysis, J. Am. Chem. Soc. 142 (2020) 14007–14022.
[41] W. Wang, Y. Tao, L. Du, Z. Wei, Z. Yan, W.K. Chan, Z. Lian, R. Zhu, D.L. Phillips, G. Li, Femtosecond time-resolved spectroscopic observation of long-lived charge separation in bimetallic sulfide/g-C_3N_4 for boosting photocatalytic H_2 evolution, Appl. Catal. B 282 (2021), 119568.
[42] A. Yamakata, T.-a Ishibashi, H. Kato, A. Kudo, H. Onishi, Photodynamics of $NaTaO_3$ catalysts for efficient water splitting, J. Phys. Chem. B 107 (2003) 14383–14387.
[43] H.N. Ghosh, J.B. Asbury, Y. Weng, T. Lian, Interfacial electron transfer between Fe(II)$(CN)_6^{4-}$ and TiO_2 nanoparticles: direct electron injection and nonexponential recombination, J. Phys. Chem. B 102 (1998) 10208–10215.
[44] A. Yamakata, T.-a Ishibashi, H. Onishi, Water- and oxygen-induced decay kinetics of photogenerated electrons in TiO_2 and Pt/TiO_2: a time-resolved infrared absorption study, J. Phys. Chem. B 105 (2001) 7258–7262.
[45] S. Cao, H. Li, T. Tong, H.-C. Chen, A. Yu, J. Yu, H.M. Chen, Single-atom engineering of directional charge transfer channels and active sites for photocatalytic hydrogen evolution, Adv. Funct. Mater. 28 (2018), 1802169.
[46] N.S. Han, H.S. Shim, J.H. Seo, S.Y. Kim, S.M. Park, J.K. Song, Defect states of ZnO nanoparticles: Discrimination by time-resolved photoluminescence spectroscopy, J. Appl. Phys. 107 (2010), 084306.
[47] J. Yuan, X. Liu, Y. Tang, Y. Zeng, L. Wang, S. Zhang, T. Cai, Y. Liu, S. Luo, Y. Pei, C. Liu, Positioning cyanamide defects in g-C_3N_4: engineering energy levels and active sites for superior photocatalytic hydrogen evolution, Appl. Catal. B 237 (2018) 24–31.
[48] J. Fu, B. Zhu, C. Jiang, B. Cheng, W. You, J. Yu, Hierarchical porous O-doped g-C_3N_4 with enhanced photocatalytic CO_2 reduction activity, Small 13 (2017), 1603938.
[49] Z. Wei, M. Liu, Z. Zhang, W. Yao, H. Tan, Y. Zhu, Efficient visible-light-driven selective oxygen reduction to hydrogen peroxide by oxygen-enriched graphitic carbon nitride polymers, Energy Environ. Sci. 11 (2018) 2581–2589.
[50] J. Jiang, X. Wang, Y. Liu, Y. Ma, T. Li, Y. Lin, T. Xie, S. Dong, Photo-Fenton degradation of emerging pollutants over Fe-POM nanoparticle/porous and ultrathin g-C_3N_4 nanosheet with rich nitrogen defect: Degradation mechanism, pathways, and products toxicity assessment, Appl. Catal. B 278 (2020), 119349.
[51] Z. Wei, J. Hu, K. Zhu, W. Wei, X. Ma, Y. Zhu, Self-assembled polymer phenylethnylcopper nanowires for photoelectrochemical and photocatalytic performance under visible light, Appl. Catal. B 226 (2018) 616–623.
[52] Y. Pan, W. Hu, D. Liu, Y. Liu, C. Liu, Carbon nanotubes decorated with nickel phosphide nanoparticles as efficient nanohybrid electrocatalysts for the hydrogen evolution reaction, J. Mater. Chem. A 3 (2015) 13087–13094.